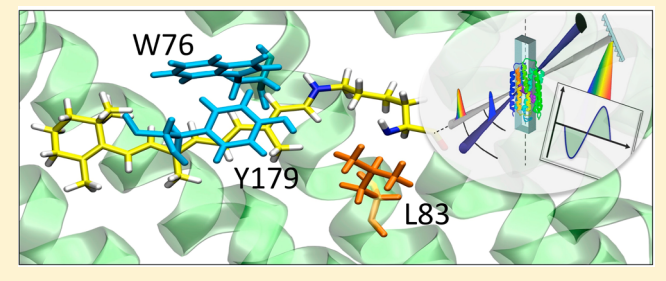


Fluorescence Enhancement of a Microbial Rhodopsin via Electronic Reprogramming

María del Carmen Marín,^{†,‡,}◆ Damianos Agathangelou,^{§,}◆ Yoelvis Orozco-Gonzalez,^{‡,||} Alessio Valentini,[⊥] Yoshitaka Kato,[#] Rei Abe-Yoshizumi,^{#,∇} Hideki Kandori,^{#,∇} Ahreum Choi,[○] Kwang-Hwan Jung,[○] Stefan Haacke,^{*,§} and Massimo Olivucci^{*,†,‡,||}

Supporting Information

ABSTRACT: The engineering of microbial rhodopsins with enhanced fluorescence is of great importance in the expanding field of optogenetics. Here we report the discovery of two mutants (W76S/Y179F and L83Q) of a sensory rhodopsin from the cyanobacterium Anabaena PCC7120 with opposite fluorescence behavior. In fact, while W76S/Y179F displays, with respect to the wild-type protein, a nearly 10-fold increase in red-light emission, the second is not emissive. Thus, the W76S/Y179F, L83Q pair offers an unprecedented opportunity for the investigation of fluorescence enhancement in microbial



rhodopsins, which is pursued by combining transient absorption spectroscopy and multiconfigurational quantum chemistry. The results of such an investigation point to an isomerization-blocking electronic effect as the direct cause of instantaneous (subpicosecond) fluorescence enhancement.

INTRODUCTION

Microbial rhodopsins have been instrumental for the development of optogenetics. In fact, when certain rhodopsins are expressed in neurons, light can be used to activate, inhibit, and even visualize neuronal activity. Indeed, few rhodopsins have been reported to exhibit a weak fluorescence, 2-4 a property that is being harnessed to develop superior action potential visualization techniques. ^{2,3,5} The understanding of the factors determining rhodopsin fluorescence is the target of the present work as a high fluorescence intensity is a prerequisite for the development of voltage sensors.^{2,4,6}

Archaerhodopsin 3 (Arch3)2 from the dead sea archaebacterium Halorubrum Sodomense, is a fluorescent microbial rhodopsin that is currently employed to visualize action potentials in neurons with space and temporal resolution. 5,7-10 However, its fluorescence is very dim (ca. 0.001 quantum yield), and three photons must be absorbed to generate one emitted photon. Furthermore, since the emission is not due to the dark adapted (DA) state but to a photocycle intermediate formed only milliseconds after photoexcitation, Arch3 has a

limited temporal resolution. Finally, Arch3 proton pumping activity partially silences the action potential signal.⁹

In order to overcome the limitations outlined above, one could look for Arch3 variants^{5,8,10} or for variants of other microbial rhodopsins^{4,7,11} displaying enhanced fluorescence intensity. The first approach has yielded, for instance, QuasAr1,8 QuasAr2,8 Archer,7 and Archon112 with the first displaying a remarkable 19-fold fluorescence increase generated by a one-photon process. The second approach has instead been applied to a rhodopsin from Gleobacter violaceous and yielded a mutant displaying a ca. 0.01 fluorescence quantum yield. 11 A third approach involves the use of cyaninebased chromophore analogues, but it has the disadvantage of not using the natural chromophore. ¹³ In spite of this progress, obtained through random or systematic mutagenesis, no attempt to unveil the mechanism behind emission enhancement has been reported. As a consequence, our ability to

Received: September 1, 2018 Published: December 11, 2018

[†]Biotechnology, Pharmacy and Chemistry Department, University of Siena, Siena 53100, Italy

^{*}Chemistry Department, Bowling Green State University, Bowling Green, Ohio 43403, United States

[§]University of Strasbourg—CNRS, Institute of Physics and Chemistry of Materials of Strasbourg, 67034 Strasbourg, France

Université de Strasbourg, USIAS Institut d'Études Avanceés, 67083 Strasbourg, France

¹Theoretical Physical Chemistry, UR Molsys, University of Liège, Liège, Belgium

Department of Life Science and Applied Chemistry, Nagoya Institute of Technology, Showa-ku, Nagoya 466-8555, Japan

 $^{^{}abla}$ OptoBioTechnology Research Center, Nagoya Institute of Technology, Showa-ku, Nagoya 466-8555, Japan

Operatment of Life Science and Institute of Biological Interfaces, Sogang University, Sogang 04107, South Korea

search rationally for highly fluorescent rhodopsins remains impaired.

In the present combined experimental and theoretical study, we consider the second approach by focusing on Anabaena Sensory Rhodopsin (ASR), a light sensor from the fresh water eubacterium *Anabaena*. ^{14–16} ASR exhibits a dim fluorescence ¹⁷ similar to Arch3 but has only a weak (inverse) proton pumping activity. Furthermore, ASR exists in two forms; all-*trans* ASR (ASR_{AT}) and 13-*cis* ASR (ASR_{13C}), which can be interconverted with light of different wavelengths. Such bistability (i.e., photochromism) is an attractive feature as it provides the basis for engineering photoswitchable fluorescent probes. ¹⁸ Finally, the X-ray crystallographic structure of ASR is available, ¹⁶ making possible the construction of realistic computer models of both wild type (WT) forms, their isomers, and their mutants.

Below we report on the accidental discovery of two ASR mutants featuring, with respect to WT, DA states with opposite fluorescence variations. In fact, W76S/Y179F displays an almost one order of magnitude enhanced fluorescence, while L83Q displays a fluorescence slightly larger than the WT but a shorter excited state lifetime (ESL). By using transient absorption spectroscopy (TAS) and quantum mechanics/ molecular mechanics (QM/MM) models based on multiconfigurational quantum chemistry (MCQC), we show that the ESL and, likely, the fluorescence intensity, is controlled by the changes in the electronic character along the first singlet excited state (S₁) potential energy surface (PES) of ASR. Indeed, the models show that the increased mixing between charge transfer and diradical characters along the S₁ isomerization path is responsible for the increase in fluorescence of W76S/Y179F. The same models show that the ESL decrease of L83Q originates from a dramatic decrease of such mixing. The QM/MM model analysis shows that specific electrostatic and steric interactions control the charge transfer/diradical mixing opening a path to the rational engineering of highly fluorescent rhodopsins.

■ METHODS

Sample Preparation and Spectroscopy. ASR proteins were expressed in *E. coli*, prepared according to the reported protocol ¹⁹ and solubilized in buffer (200 mM NaCl, 25 mM Tris-HCl, 0.02% DDM, pH 7.0). The steady state absorption spectra of the DA and light-adapted (LA) proteins were recorded by using a PerkinElmer "Lambda 950" UV/vis spectrometer. DA samples were prepared by incubation in the dark for at least 12 h at room temperature, while the LA samples, orange-adapted (OA) or green-adapted (GA), were exposed to light illumination for 30 min using Luxeon LEDs "LXHL-PL01" (590 \pm 10 nm) or "LXHL-NE98" (500 \pm 15 nm), respectively.

The fluorescence emission spectra for DA, OA, and GA states were recorded by using a homemade static fluorescence setup. ¹⁵ Replacement of the excited volume, required for preserving the DA state, was achieved by circulation of the sample, using a peristaltic pump through a close circuit consisting of a 0.5 mm path length flow cell and a 2 mL vial serving as sample reservoir. A nitrogen cooled CCD (–120 °C, PyLoN, Princeton Instr.) mounted on an imaging spectrometer (SP-2300i, Princeton Instr.) was used for detection of the signal covering the 550–1050 nm spectral range with 4 nm resolution. See the SI for more details.

TAS was carried out with sub-80 fs temporal resolution at 1 kHz repetition rate (system described elsewhere 20). A homemade noncollinear parametric amplifier was used for delivering sub-60 fs excitation pulses at the wavelength of interest, while a NIR broad band probe pulse (850–1400 nm) was produced by focusing $\sim\!0.7~\mu\mathrm{J}$ of the 800 nm fundamental beam in a 4 mm thick YAG crystal. 21 The

probe beam was dispersed in an Acton "SP2156" spectrograph, and the single pulse spectra at 1 kHz were recorded by a Hamamatsu IR head sensor (G11608–256).

Determination of the LA-dependent isomer content was done after retinal oxime extraction, by performing High Performance Liquid Chromatography. Patinal oximes were resolved using a Dionex UltiMate 3000 System, equipped with a Zorbax SIL 70 Å 4.6 \times 250 mm–5 $\mu \rm m$ column (see detailed protocol in the SI).

Computations. The QM/MM models were built using the Automatic Rhodopsin Modeling (ARM) protocol²² (see Figure 1A

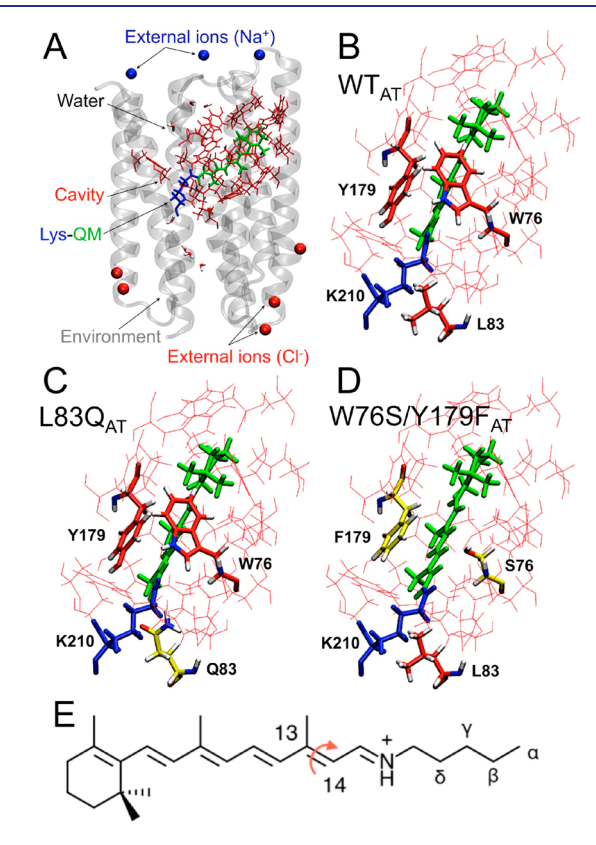


Figure 1. QM/MM models. (A) General structure of the ASR model. The protein environment is colored in gray with external counterions in blue (Na⁺) and red (Cl⁻). The region hosting of the retinal chromophore is colored in red with the Lys210-chromophore system in blue-green. Chromophore hosting region for the all-trans isomers of (B) WT (ASR_{AT}), (C) L83Q, and (D) W76S/Y179F. The variable cavity residues 76, 83, and 179 are shown in tube representation. (E) All-trans retinal chromophore. The curly arrow indicates the $\rm C_{13}$ —C $_{14}$ isomerizing double bond, and the greek letters are the atoms of the Lys210 side chain.

and the SI for details). ARM employs the complete active space self-consistent field $(CASSCF)^{23}$ MCQC method combined with the Amber molecular mechanics force field to obtain ground state (S_0) QM/MM models of rhodopsins semiautomatically in a standardized fashion. Vertical excitation energies are then computed using multiconfigurational second-order perturbation theory $(CASPT2)^{24}$ to recover the dynamic electron correlation missing by the CASSCF wave function.

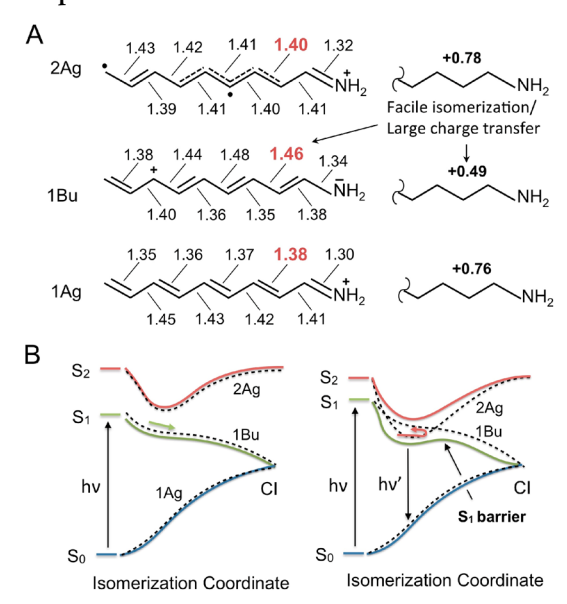
Excited state reaction paths are documented by computing relaxed scans driven by the $C_{12}-C_{13} = C_{14}-C_{15}$ dihedral angle of the rhodopsin chromophore (Figure 1E). The S_1 dynamics is instead investigated by computing semiclassical Franck–Condon (FC) trajectories, namely, deterministic surface-hop trajectories released on S_1 PES starting from the S_0 equilibrium structure with zero initial velocities. All QM/MM energy, gradient, relaxed scan, and FC trajectory calculations were carried out using interfaced Molcas²⁵

quantum chemistry and Tinker²⁶ molecular mechanics/dynamics packages.²⁷

■ RESULTS AND DISCUSSION

Bonding in the Excited Electronic State. Here we introduce the theoretical framework necessary to discuss the results presented below. Since a detailed discussion can be found in recent publications, ^{28,29} we limit ourselves to a summary of the properties of the first three PESs of a gas-phase model of the rhodopsin chromophore featuring five conjugating double-bonds (PSB5). ^{17,29} Scheme 1A shows the

Scheme 1. Electronic and Bonding Structure of the Retinal Chromophore^a



"(A) Left. Resonance formula associated to the electronic characters (1Ag, 1Bu, and 2Ag) dominating the S_0 , S_1 , and S_2 equilibrium structures of PSB5. The bond lengths are given in Å (see left part), and the total charge of the displayed moiety (see right part) is indicated in bold. (B) Schematic S_0 , S_1 , and S_2 energy profiles along the S_1 PES path driving the chromophore S_1 isomerization. An S_1 PES dominated by a 1Bu character (left) is associated with a barrierless path, while a mixed 1Bu/2Ag character (right) is associated with the presence of a barrier along the path. The dashed energy profiles represent the energy of diabatic states corresponding to "pure" 1Bu and 2Ag electronic characters.

electronic characters dominating the S_0 , S_1 , and S_2 equilibrium structures of PSB5 when this is subject to a planarity constraint. These are labeled 1Ag, 1Bu, and 2Ag (consistent with the electronic terms of a homologous all-*trans* polyene with C_{2h} symmetry). 28,30 S_1 has a 1Bu character characterized by a positive charge spread (i.e., transferred) toward the $H_2C=CH-$ end of the PSB5 framework. This is qualitatively different from the 1Ag character of S_0 , which has the positive charge localized on the $-C=NH_2$ terminal moiety. In contrast, the second singlet excited state (S_2) has 2Ag character associated with a diradical, rather than charge transfer, structure, and features, similar to S_0 , a positive charge mostly located on the $-C=NH_2$ moiety.

In the present work, we take the 1Ag, 1Bu, and 2Ag charge distributions as a reference to follow how the electronic character changes along the S_1 PESs (e.g., along a reaction path or trajectory). To do so, we compute the charge of a suitable

chromophore moiety and track its variations along the PES. For example, as shown in the right part of Scheme 1A and consistently with the resonance formulas, the -CH-CH- $CH-CH-NH_2$ moiety has a large positive charge (ca. + 0.8) in regions with dominating 1Ag and 2Ag characters but a smaller charge (ca. + 0.5) when the 1Bu charge transfer character is dominating. Second, the same charge provides information on the nature of the π -bonding along the path. This is shown in Scheme 1A where we report the bond lengths of the equilibrium reference structures. A structure dominated by a 1Bu character displays inverted double and single bond lengths facilitating double bond isomerization (see values in red). In contrast, in a structure with 2Ag character, the double bonds are only weakened (i.e., partially broken) and thus feature a residual torsional energy barrier restraining double bond isomerization. Third, one can use the charge distribution to track the electronic coupling between two PESs. For instance, the fact that along a trajectory the S_1 and S_2 charges of the -CH-CH-CH-NH, moiety change in a mirrorimage like fashion 29,31 indicates that the S_1 and S_2 PESs are electronically coupled. In other words, the PESs exchange 1Bu (reactive) and 2Ag (nonreactive) character. This occurs in the presence of an avoided crossing region as the one illustrated in Scheme 1B. In such a scheme, the 1Bu and 2Ag electronic characters are regarded as diabatic states (i.e., states with pure characters), which mix to generate the S₁ and S₂ adiabatic states. In the left diagram, the S2 and S1 PESs remain dominated by the same diabatic state. In contrast, the right diagram displays a situation where the diabatic states cross twice and, therefore, the S₁ PES shows regions dominated by a 2Ag character. The electronic states driving the photoisomerization of model retinal chromophores have originally been described by Josef Michl and Vlasta Bonacić Koutecky. 30,32

Below we assume that the ESL is determined by the chromophore S_1 reactivity. In other words, the isomerization motion on S_1 , leading to fast nonradiative decay through a CI between the S_1 and S_0 PESs, is held responsible for the subpicosecond ESL and the low fluorescence quantum yield (QY). Consistently, the presence of an energy barrier along the S_1 isomerization path would increase the ESL and QY proportionally to the barrier magnitude.

Spectroscopy and Reactivity Studies. The observed absorption spectra of the DA, OA, and GA states of ASR are reported in Figure 2A for the WT and W76S/Y179F and L83Q³³ mutants. As shown in Figure 2B, the observed trend in absorption maxima (λ^a_{\max}) is reproduced by using all-trans QM/MM models to compute the corresponding vertical excitation energies for the S₀ \rightarrow S₁ transition ($\Delta E_{\text{S1-S0}}$). The blue-shifted λ^a_{\max} of W76S/Y179F and L83Q (6 and 4 kcal/mol, respectively, in terms of $\Delta E_{\text{S1-S0}}$) must originate from changes in the interactions between protein and chromophore (see Figure 1B–D). More specifically, the change from leucine (L) to glutamine (Q) in L83Q and the change from tryptophan (W) to serine (S) and tyrosine (Y) to phenylalanine (F) in W76S/Y179F must destabilize S₁ with respect S₀ (or stabilize S₀ with respect to S₁).

In Figure 2C we also report the fluorescence spectra of DA WT, L83Q, and W76S/Y179F. Also GA and OA spectra are shown for the W76S/Y179F mutant. Experimental spectra are rescaled in order to correct for the sample-dependent absorbance values. The integrated fluorescence intensity is thus proportional to the fluorescence QY (see SI). Remarkably,

Journal of the American Chemical Society

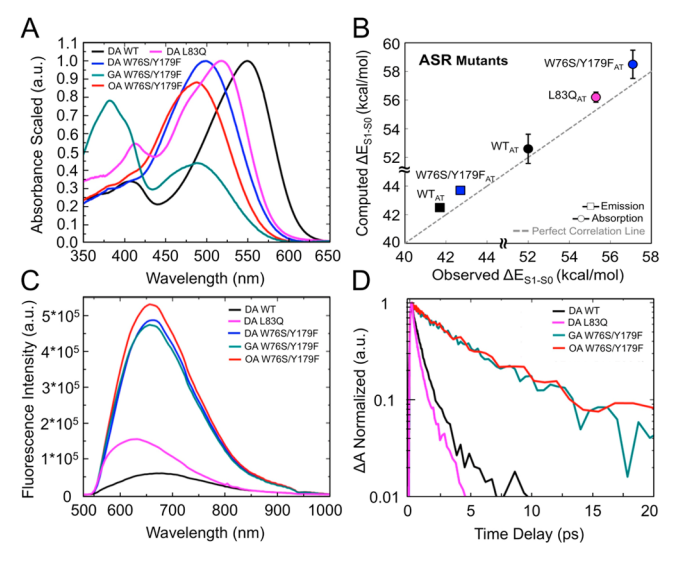


Figure 2. Steady state spectra and excited states dynamics. (A) Scaled absorption spectra of light-adapted (OA and GA) W76S/Y179F mutant and dark-adapted (DA)WT, W76S/Y179F, and L83Q mutants of ASR. Light-adaptation was carried out either with an orange or green LED. (B) Comparison between simulated all-trans and observed $\lambda^a_{\rm max}$ (circles) and $\lambda^f_{\rm max}$ (squares) values for the DA state. Deviation bars for the computed excitation energy values are shown as black segments. The excitation energy errors fall in the 0.5–1.5 kcal/mol range typical of ARM. (C) Steady state emission of DA WT ASR, DA L83Q ASR, DA, OA, and GA W76S/Y179F mutant of ASR. (D) Comparison of the SE kinetic traces of WT (black trace), L83Q (pink trace), and W76S/Y179F (GA green trace and OA red trace).

the data show that the QY of W76S/Y179F is ca. one order of magnitude higher than that of WT and, therefore, not far from that of certain improved Arch3 mutants. The In Figure 2B we show that the same all-trans QM/MM models reproduce the observed trend in emission maxima (λ_{\max}^f). In fact, the ΔE_{S1-S0} (see Table S3) computed at the corresponding S1 equilibrium structure (see MINWT and MINW76S/Y179F in Figure 3C,E) yield a λ_{\max}^f of 758 nm for WT and 744 nm for W76S/Y179F. However, these values do not account for the kinetic energy of the molecule. To do so, we compute the average ΔE_{S1-S0} values along the FC trajectories of Figure 4C,E starting 15 fs after the initial relaxation. The computed λ_{\max}^f values of 672 nm for WT and 654 nm for W76S/Y179F are closer to the observed values of 674 nm for WT and 658 nm for W76S/Y179F.

As displayed in Figure 2D and Table 1, the ESL values are critically dependent on the mutations, as determined from the stimulated emission (SE) decay traces. We find values of 0.48, 0.86, and 5.7 ps for L83Q, WT, and W76S/Y179F, respectively (global fit of the entire SE data set, see SI). Comparing W76S/Y179F and WT, the measured and spectrally integrated steady-state emission intensities (see SI for details) are almost proportional to the average ESLs, as expected since the fluorescence QY is $\Phi = \text{ESL*}k_{rr}$ with k_r being the radiative rate. L83Q shows a larger QY despite an almost 2-fold reduction of the ESL, indicating that L83Q has a higher radiative rate than WT (see SI for details).

A complication arises for W76S/Y179F, which presents a light-adaptation-dependent isomer content, including the noncanonical 9-cis or 7-cis isomers, with a relative amount comparable to all-trans. Importantly, in the GA state a relative

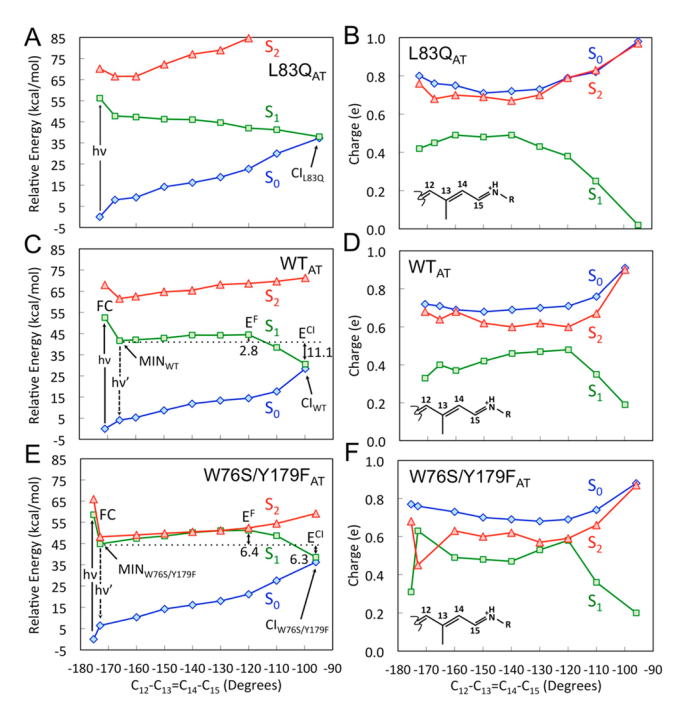


Figure 3. C_{13} = C_{14} isomerization path on S_1 . (A,C,E) CASPT2// CASSCF/AMBER energy profiles along S_1 (green squares) isomerization path of L83Q, WT, and W76S/Y179F, respectively. S_0 (blue diamonds) and S_2 (red triangles) profiles along the S_1 path are also given. The S_1 is computed in terms of a relaxed scan along C_{12} - C_{13} = C_{14} - C_{15} dihedral angle. The corresponding, computed oscillator strengths are given in Figure S3. (B,D,F) Corresponding Mulliken charge variation of the -CH-CH-CH-CH-NH₂ moiety of the chromophore of L83Q, WT, and W76S/Y179F, respectively.

amount of 54% of the pair 9-cis and 7-cis isomers accumulates in S_0 absorption and was used for comparison with the OA state where the all-trans isomer is the dominant one (39%, see SI). For both the TAS and steady-state fluorescence experiments, the excitation wavelength was tuned to the lower energy tail of ground state absorption for selective excitation of all-trans isomer since its $\lambda^a_{\rm max}$ was calculated to be largest among all isomers. We find indeed that 9-cis and 7-cis isomers rather absorb in the 350–420 nm range (see Figure S12 in the SI). The SE dynamics are identical for both OA and GA light-adaptation states, even though the amount of 9-cis and 7-cis isomers almost doubles in GA. We thus conclude that in the present conditions, the ESL and the increased fluorescence emission comes mainly from the all-trans isomer.

In the following, we will show that the above all-trans QM/MM models reproduce the trends in ESLs and fluorescence intensities when they are probed via reaction paths and 200 fs FC trajectory computations.

The photochemical reactivity of WT, L83Q, and W76S/Y179F has been initially investigated by computing the all-trans to 13-cis relaxed scans connecting the FC point to the S_1/S_0 CI along the C_{13} = C_{14} twisting describing the isomerization. The resulting energy profiles are reported in Figure 3A,C,E. It is apparent that the steep S_1 potential energy profile of L83Q would accelerate the S_1 population toward the CI more effectively than the flatter WT and W76S/Y179F PESs. The results appear to be consistent with the measured ESLs, fluorescence intensities, and quantum yields (see Table 1 and panels C,D). More specifically, WT and W76S/Y179F display S_1 energy profiles (see Figure 3C,E) featuring a ca. 3 and 6

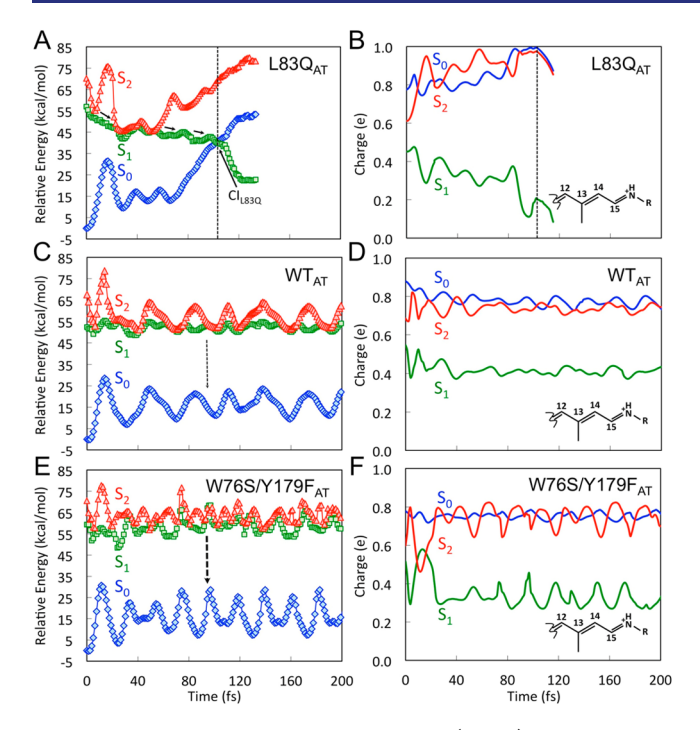


Figure 4. Trajectory computation on S_1 . (A,C,E) QM/MM FC trajectories (see main text) of L83Q, WT, and W76S/Y179F, computed at two-root state-averaged-CASSCF/AMBER level of theory and corrected at the CASPT2 level. S_0 (blue diamonds), S_1 (green squares), and S_2 (red triangles) CASPT2/CASSCF/AMBER energy profiles along the FC trajectories. The corresponding, computed oscillator strengths are given in Figure S6. (B,D,F) Corresponding Mulliken charge variation of the $-CH-CH-CH-CH-CH-NH_2$ moiety of the chromophore of L83Q, WT, and W76S/Y179F, respectively. To test the robustness of the W76S/Y179F results, the data of panels E and F have been recomputed at the S-root-state-average level (see Figure S10).

Table 1. Time Constants and Amplitudes from the Biexponential Decay of SE, Average ESLs, and Experimentally Determined Fluorescence QYs (Φ) with Respect to That of Bacteriorhodopsin (Φ_{bR}) , Determined from the Spectrally Integrated Fluorescence Intensities^a

sample	A_1	t_1 (ps)	A_2	t ₂ (ps)	ESL (ps)	$\begin{array}{c} \Phi/\\ \Phi_{bR} \end{array}$
DA L83Q	0.78	0.27 ± 0.05	0.22	1.2 ± 0.2	0.48	2.4
DA WT	0.72	0.55 ± 0.05	0.28	1.7 ± 0.2	0.86	1.1
OA W76S/ Y179F	0.60	2.8 ± 0.3	0.40	10 ± 0.8	5.7	8.7
GA W76S/ Y179F	0.40	2.1 ± 0.4	0.60	8 ± 0.7	5.7	7.6

"The fluorescence QY's are determined with bacteriorhodopsin as a reference sample (see SI). However, we refrain from quoting absolute values since the only available experimentally determined value for bacteriorhodopsin appears to be excessively high, most probably due to contributions from later photocycle intermediates.³⁴

kcal/mol isomerization barriers, respectively, leading to an increased ESL for the double mutant.

The results of 200 fs FC trajectory calculations for the all-trans models of L83Q, WT, and W76S/Y179F are given in Figure 4A,C,E, respectively. In all cases, we assume that during such a short time the trajectories describe the average evolution of population on the lowest excited states $(S_1$ and $S_2)$.³⁵ As shown in Figure 4A, L83Q reaches the photochemi-

cally relevant S_1/S_0 CI and decays to S_0 in ca. 100 fs consistently with the dominant 270 fs decay (Table 1) as well as the S_1 potential energy slope of Figure 3A (notice that FC trajectories usually decay earlier with respect to the population investigated experimentally; see Figure 9 in ref 35) In contrast, Figure 4C,E show that WT and W76S/Y179F do not reach the CI within the simulation time, consistently with the observed shortest decay time, which is, in both cases, above 500 fs and with the computed S_1 barriers in Figure 3C,E.

The computational results above are based on all-trans QM/MM models. Such models do not take into account the effect of mutations on the isomer composition of the DA state, which may be altered in the mutants. In fact, as said above, in contrast with WT and L83Q, whose DA states are dominated by the all-trans chromophore, W76S/Y179 has a more complex isomer composition (see Figure S11 and Table S4). However, as explained above, the OA and GA steady-state absorption together with the isomer compositions for both OA and GA show that the 7-cis and 9-cis isomers do not contribute to the absorption band at 490 nm. Thus, the presence of these isomers does not alter the conclusions for W76S/Y179 based on the all-trans model exclusively.

Structure and Dynamics of the Emissive Excited State Species. In the present subsection we use the all-trans QM/MM models to investigate the mechanisms at the basis of the observed and simulated fluorescence enhancement. More specifically, we provide evidence that the increase in mixing between the reactive 1Bu and nonreactive 2Ag characters introduced above correlates with the observed L83Q < WT < W76S/Y179F trend in S $_1$ ESL. In other words, we provide support for a structure of the L83Q and W76S/Y179F PESs and related dynamics consistent with the left and right diagram of Scheme 1B, respectively. 29

The comparison of panels A,C,E shows that the average S₂- S_1 energy gap along the S_1 path decreases in the order L83Q > WT > W76S/Y179F. As apparent from panels B,D,F, such changes are accompanied by changes in the positive charge distribution and, in turn, 1Bu character (see discussion). Thus, in W76S/Y179F the population moving out of the FC point, where one has a 1Bu character (i.e., the S₁ charge of the -CH-CH-CH-CH-NH2 fragment is less than in So and S_2), transits along regions where the 2Ag character of the S_1 PES increases (MIN_{W76S/Y179F} in Figure 3E) indicating character mixing and then reaches regions (ca. −120° in panel F) where the 1Bu and 2Ag characters have close weights (similar charge in S_1 and S_2). This happens at a lesser extent in WT featuring a larger 1Bu weight in S₁ and at an even lesser extent in L83Q where the charge becomes less than +0.2 and the 1Bu character is retained. This appears to be also consistent with the larger S2-S1 gap along the energy profiles of panel C, which is brought to a periodic degeneracy (see Figure 4C) only when the chromophore acquires kinetic energy.

The magnitude of the S_1 barrier (E^F in Figures 3C and 3E), and in turn, the ESL, appears to increase with the mixed 1Bu/2Ag character at the ca. -120° twisted structure (see Figures 3B,D,F), which approximates the S_1 transition state. This suggests that, in contrast to L83Q, in W76S/Y179F the S_1 and S_2 PESs are generated via avoided crossings between 2Ag and 1Bu diabatic states as illustrated in Scheme 1B left. In other words, the S_1 energy barrier at -120° would be a result of such crossing.

Journal of the American Chemical Society

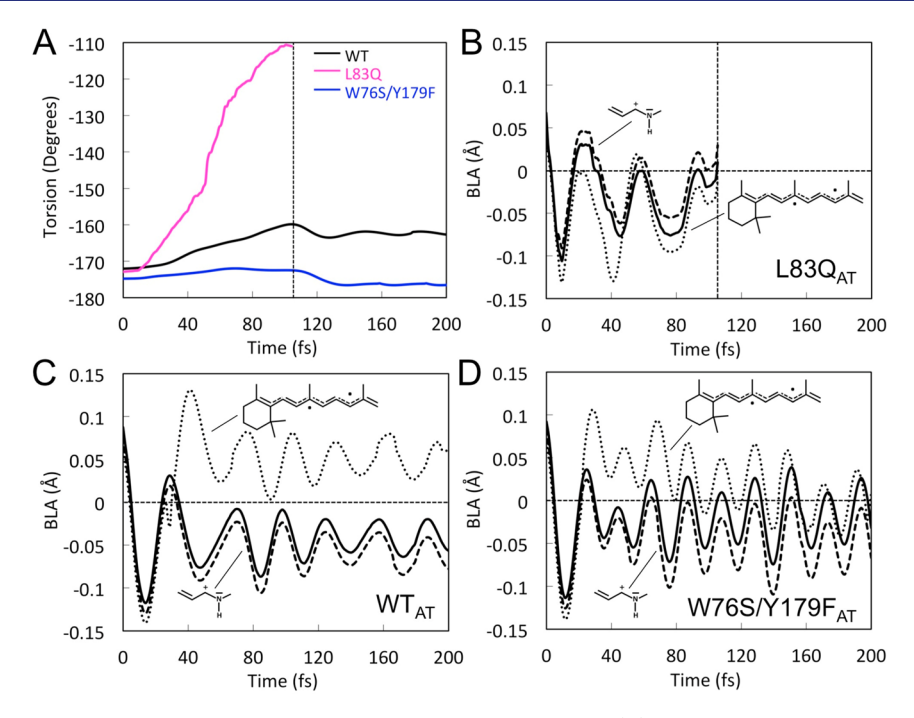


Figure 5. Geometrical variation along the L83Q, WT, and W76S/Y179F FC trajectories. (A) Evolution of the $C_{12}-C_{13}=C_{14}-C_{15}$ dihedral angle along the FC trajectories of all-trans ASR L83Q (purple), WT (black), and W76S/Y179F (blue) representing the $C_{13}=C_{14}$ isomerization. (B–D) Evolution of the total BLA (full line) and of the BLA of two specific moieties (dotted and dashed lines) for L83Q, WT, and W76S/Y179F, respectively.

The increasing 2Ag character along the S₁ energy profile in W76S/Y179F must have important consequences on the excited state dynamics. 2Ag being less reactive than 1Bu as demonstrated by the documented EF barrier, the molecular population will be temporarily trapped in S₁ causing an increase in ESL with respect, for instance, to L83Q where the 1Bu character dominates and the S_1 PES has no barrier. However, since the reaction paths of Figure 3 do not consider kinetic energy effects, we have confirmed the above conclusion via FC trajectory calculations. Consistently with literature data, 28 initially all trajectories relax along a bond-lengthalternation (BLA) stretching mode where the single bonds shrink and the double bonds expand. During BLA relaxation, which occurs within 30 fs, L83Q, WT, and W76S/Y179F enter a S_2/S_1 near degeneracy region, which is associated with the emissive species (sometimes called fluorescent state). Such region shall eventually be left to follow the C13=C14 isomerization coordinate. As anticipated above, we find that only L83Q exits such a region within the 200 fs simulation time supporting the mechanistic interpretation provided by the reaction paths (see Figure 5A).

The FC trajectories provide a detailed dynamic description of the S_1 trapping process due to the change in electronic character. In fact, in the reactive L83Q case (Figure 4A,B), the S_2 energy profile only crosses the S_1 energy profile in the 20 to 50 fs time segment and then becomes destabilized. Thus, as shown in Figure 4B, the system remains dominated by a 1Bu reactive character and it is not trapped in S_1 . However, the trapping occurs in WT and W76S/Y179F (for WT see also our previous report²⁹). In these cases, the S_2 and S_1 profiles cross (or couple) periodically generating "islands" with increased nonreactive 2Ag character. These islands are characterized by BLA oscillations (see also Figure 5), which modulate the S_1 and S_2 gap and the associated 1Bu/2Ag character mixing. This is confirmed by the $S_0 \rightarrow S_1$ oscillator strength progression

(Figure S6) showing oscillations of a lower magnitude in WT than in W76S/Y179F. The described behavior is supported by the fact that the S2 and S1 positive charge on the reference $C_{12}-C_{13}=C_{14}-C_{15}=NH_2$ fragment display mirror-image variations (see Figure 4D,F).²⁹ As a consequence, due to the change in the corresponding electronic/bonding characters such motion hampers the unlocking of the $C_{13}=C_{14}$ double bond and, as a consequence, the reactivity of the S₁ chromophore. The frequency and depth of such crossingrecrossing events is larger for W76S/Y179F, and this is attributed to the S₂/S₁ degeneracy, which is already accomplished at the reaction path level (compare Figure 3C,E). Consistently, in W76S/Y179F the S₂ state becomes more stable than S₁ periodically each 30 fs. This does not happen in WT where the S2 state only "touches" the S1 energy profile with about the same frequency.

The formation of unreactive "islands" can also be documented structurally. For instance, in Figure 5A we report the evolution along the dihedral angle describing the isomerization of the $C_{13}=C_{14}$ double bond. The dihedral reaches the typical -110° value of a CI exclusively for L83Q. However, the generation of unlocked double bonds prone to isomerize (i.e., via double-bond-single-bond inversion) can be tracked by plotting the BLA value of specific chromophore fragment. Accordingly, in Figures 5B-D we report the evolution of the BLA value of a suitable β -ionone containing fragment. It oscillates about a completely inverted BLA value in L83Q (i.e., negative average BLA values) but not in WT and W76S/Y179F (i.e., positive average BLA values). As mentioned above, the DA state of the fluorescent ASR mutant W76S/Y179F is not dominated by a single all-trans isomer, which, in fact, only accounts for 30% of the total population. Such state also contains 15% of 13-cis and 18% of 11-cis isomers and 36% of a mixture of 9-cis and 7-cis isomers (see Table S4). As said above, the latter can be disregarded since they are not excited in both the steady-state fluorescence and TAS experiments (see SI), but the contribution of 13-cis and 11-cis isomers needs to be discussed. We have used the same type of QM/MM model to investigate their photoisomerization dynamics via FC trajectory calculations. As shown in Figure S9, the 13-cis and 11-cis isomer reach a CI within 200 fs, a component that is not observed in the SE decay since the pump wavelength favors all-trans excitation. Since, the fluorescence spectra were recorded with the same excitation wavelength, and the increase in fluorescence quantum yield matches the ESL increase of W76S/Y179F with respect to WT, we conclude that these isomers do not contribute to the observed fluorescence. However, the 9-cis and, most likely, the 7-cis isomers would contribute with the same mechanism operating in the all-trans isomer (see the SI).

However, again, the steady state absorption spectra of OA and GA states strongly suggest that both isomers absorb in the region between 350 and 400 nm, are not excited, and are not presented in the TAS and static fluorescence measurements (see SI).

Residue-Level Modulation of Excited State Emission.

We now provide information on how emissive PES regions (i.e., the islands described above) get stabilized (or destabilized) via electrostatic and/or steric interactions with specific residues. The L83Q, WT, and W76S/Y179F models indicate that the increase in ESL is due to the appearance of an S_1 energy barrier at ca. -120° twisting whose magnitude increases with the 1Bu/2Ag mixing developing along the S₁ PES. However, it is unclear if such variations are caused by changes in the electrostatic field acting on the chromophore or by changes in the chromophore geometrical progression (i.e., in the isomerization coordinate). To investigate the electrostatic effect we recomputed the energy profile of Figure 3A (i.e., for L83Q) for the isolated (i.e., in vacuo) chromophore taken with its protein geometry. The comparison between Figures 6A and 3A (or the dashed lines in Figure 6A) demonstrates that the change in protein electrostatics is fully responsible for the absence of a barrier in L83Q. Indeed, in the absence of protein electrostatic effects, the energy profile of L83Q appears to be very similar to the one detected along the WT and W76S/Y179F S₁ PESs when the protein is present. This behavior must be connected with the charge evolution of Figure 6B, which shows a marked difference when plotted in the presence and absence of the protein. In fact, it can be seen that between -140° and -120° the S₁ charge evolution displays a fast increase of 1Bu/2Ag mixed character in the isolated chromophore.

Remarkably, the same L83Q barrier induction effect is seen in the presence of a protein environment where the charges of the Q residue in position 83 are set to zero (see Figure S4). This is also consistent with the fact that it is sufficient to replace the polar Q residue with the apolar L residue (or with a "residue" with zero charges) to create the barrier akin to ${\rm ASR}_{\rm AT}$, which may, in part, be due to the relocation of the remaining cavity charges.

The removal of the S_1 barrier at the -120° twisted transition state can thus be directly connected to the interaction between the chromophore orientation, its torsion-induced charge translocation, and the Q83 side chain. While we cannot presently provide a quantitative analysis, our computations reveal two effects. First (see Figure 7A), there is an evident reorientation of the π -conjugated chain along the reaction path and the side-chain of the Q83 residue (compare the torsional

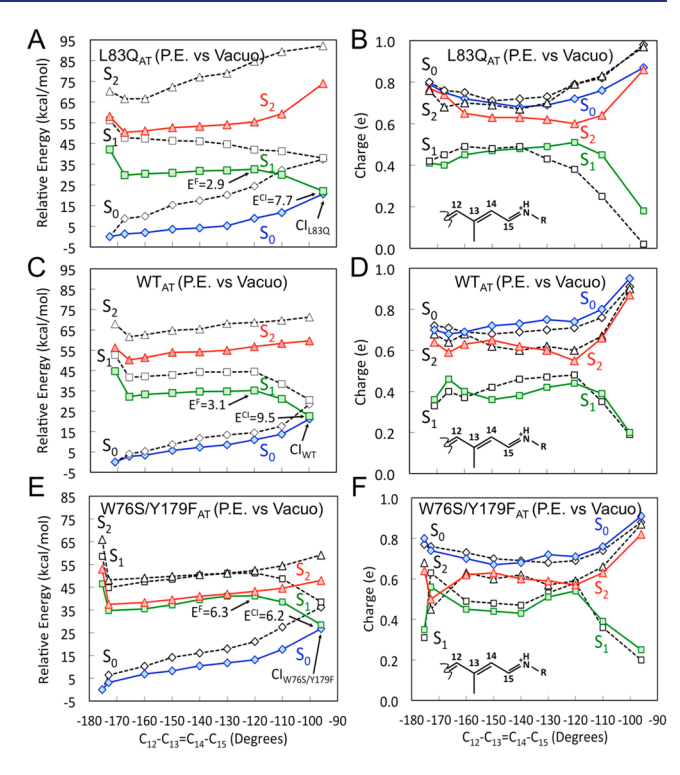


Figure 6. Energy profiles along the S_1 isomerization paths of Figure 3 for the chromophore *in vacuo*. (A,C,E) CASPT2//CASSCF/AMBER energy profiles for the S_1 state (green squares) of L83Q, WT, and W76S/Y179F, respectively. S_0 (blue diamonds) and S_2 (red triangles) profiles along the same path. (B,D,F) Corresponding Mulliken charge variation of the $-CH-CH-CH-CH-NH_2$ moiety of the chromophore of L83Q, WT, and W76S/Y179F, respectively. In all panels, the dashed energy profiles represent the corresponding energy profiles of the entire protein models (i.e., from Figure 3).

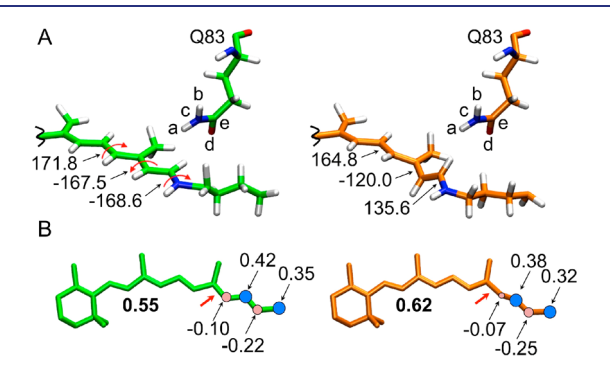


Figure 7. Geometrical and charge distribution variations along the S_1 isomerization path of L83Q (see Figure 3A). (A) Geometrical variation documented by three critical dihedral angles (curly arrows). The left structure corresponds to the second point along the energy profile of Figure 3A (i.e., the point corresponding to MIN $_{\rm WT}$ and MIN $_{\rm W76S/Y179}$), while the right structure is the "transition state" structure featuring a $-120~^{\circ}{\rm C}_{12}-{\rm C}_{13}$ = ${\rm C}_{14}-{\rm C}_{15}$ dihedral angle. (B) Charge distribution data for the same two structures.

deformation of the left structure corresponding to the second point along the path of Figure 3A with the "transition state" structure featuring a -120° twisted $C_{13} = C_{14}$ double bond). Second (see Figure 7B), the charge transfer character is increasing along the path thereby enhancing the intensity of the interaction between chromophore and the dipolar Q83 side-chain. Our results suggest that, in the presence of the Q83 side-chain charges, the "transition state structure" gets

stabilized on S₁ with respect to the earlier structures along the path, and this leads to the disappearance of the S_1 barrier. However, such electrostatic stabilization is not an obvious effect as it depends on the exact reorientation of the chromophore during the isomerization and on the change in 1Bu character.

In Figure 6C-E, we report the same in vacuo analysis for WT and W76S/Y179F. Remarkably, in both cases there are no qualitative changes in the energy profiles indicating that the S₁ barrier is not associated to electrostatic interaction but that it is an intrinsic feature of the chromophore geometrical changes along the two paths. This conclusion is also valid for the S_2/S_1 degeneracy region of W76S/Y179F, which is maintained after removal of the protein electrostatic field. Furthermore, as we show in the SI, it is possible to transform the WT S_2 , S_1 , and S_0 energy profiles into W76S/Y179F-like energy profiles by simply changing the backbone dihedral angles along the WT reaction coordinate to the corresponding W76S/Y179F values. This is remarkable because those are limited changes that indicate the fluorescent tuning in rhodopsins might be achieved also through subtle geometrical effects.

CONCLUSIONS

Above we have looked at the origin of experimentally observed fluorescence QY and ESL variations in the DA state of ASR. While mutants of other microbial rhodopsins (e.g., bacteriorhodopsin and proteorhodopsin)³⁶ display an ESL increase, in our study we have reported on an electronic state mixing mechanism for ESL and fluorescence QY enhancement. In order to do so, the stationary and transient spectral parameters for WT and for L83Q and W76S/Y179 have been measured. Remarkably, while both mutants display, with respect to WT, blue-shifted absorption maxima, the measurements reveal opposite ESL changes. Indeed, while it is found that the W76S/Y179F mutant has a picosecond lifetime with a fluorescence QY not too far from the improved Arch3 mutants applied in optogenetics, L83Q fluoresces very weakly and undergoes all-trans to 13-cis isomerization on a ca. 200 fs time scale.

By using the ASR_{AT} isomer as a DA state model, we show that MCQC-based QM/MM models are capable to reproduce the observed trends in absorption, emission, and ESL indicating their suitability for mechanistic studies. Accordingly, reaction path and trajectory computations show, consistently, that the observed change in ESL is due to an opposite change in charge transfer character of the S_1 state of the molecule. Such changes that can be described as an increase in unreactive 2Ag diradical character along the L83Q, WT, and W76S/ Y179F series do not regard the FC region but a critical segment of the reaction path or trajectory where the rhodopsin chromophore is significantly twisted. This mechanism is different from others that have been proposed for ESL increase in microbial rhodopsins.³⁷ Notice that a 2Ag/1Bu degeneracy has been reported for the retinal chromophore in solution in both computational³⁸ and experimental³⁹ studies.

While the nature of the electronic character variation causing the fluorescence enhancement is found to be consistently the same, QM/MM model analysis points to very different residue-level mechanisms responsible for such variations. In other words, the residue replacements in L83Q and W76S/ Y179F appear to operate via dramatically different effects. The L83Q to WT variation is dominated by an electrostatic effect,

while the WT to W76S/Y179F variation is controlled by steric effects: a change in the details of the isomerization coordinate.

Even if two mutants form a limited set, the consistency of the experimentally observed and simulated quantities confer a high significance to the described findings, which have a direct impact in the design of highly fluorescent rhodopsins. The most significant of these finding is the undeniable intrinsic complexity of the regulation of a basic spectroscopic property such as light emission. In the presented examples, such complexity shows up dramatically even upon a one-two residue replacement and discourages the extraction of simple "rules-of-thumb", which are sometimes introduced, in our opinion inappropriately, in the context of color tuning. However, our study suggests that the extension of the present study to an entire array of mutants may reveal if a rapidly computable structure such as the -120° TS located above, and the actual S_1/S_2 degree of mixing, can be used for practical in silico screening of fluorescent mutants.

As stressed above, the increase in ESL is a factor necessary for employing rhodopsins as fluorescence reporters. Another factor is the sensitivity to voltage changes across the membrane. While a robust study of voltage sensitivity of the ASR_{AT} W76S/Y179F mutant goes beyond the scope of the present work, in the SI we report the result of a preliminary computational investigation. In such study, we have probed the sensitivity of the λ_{\max}^f and oscillator strength values of the ASR_{AT} W76S/Y179F QM/MM model to an increase/decrease in the number of external ions in the inner/outer surfaces of the protein (see Figure 1A). The result indicates that the λ_{\max}^t is sensitive to the change in external ion concentration, which is assumed to provide a suitable model for voltage variation. Accordingly, ASR_{AT} W76S/Y179F or its variants may lead to promising voltage reporters for observing either the change in fluorescence intensity at a specific wavelength or the change in λ_{\max}^{t} as a function of time.

ASSOCIATED CONTENT

Supporting Information

The Supporting Information is available free of charge on the ACS Publications website at DOI: 10.1021/jacs.8b09311.

> QM/MM model, computation and experimental details, and voltage sensitivity (PDF)

> QM/MM ground state optimized structures of ASR WT (PDB), L83Q (PDB) and W76S/Y179F mutants (PDB)

AUTHOR INFORMATION

Corresponding Authors

*molivuc@bgsu.edu

*stefan.haacke@ipcms.unistra.fr

Hideki Kandori: 0000-0002-4922-1344 Massimo Olivucci: 0000-0002-8247-209X

Author Contributions

◆María del Carmen Marín and Damianos Agathangelou contributed equally.

Notes

The authors declare no competing financial interest.

ACKNOWLEDGMENTS

The research has been supported by the following grants NSF CHE-CLP-1710191 and NIH GM126627 01. M.O. is grateful for a USIAS 2015 grant. S.H. is grateful for support by the French-German ANR-DFG grant Femto-ASR (ANR-14-CE35-0015-01), by the Labex NIE (ANR-11-LABX- 0058_NIE), and by "région Alsace" (Ph.D. grant D.A.). The France-Korea collaboration is supported by CNRS in the framework of the "LIA NanoFunc". H.K. is grateful for support from MEXT (Japan) and CREST-JST (Japan). K.H.J. is grateful for grant NRF-2016R1A6A3A11934084 (South Korea). We thank Dr. Luca De Vico for technical help with the computations and for valuable discussions. We thank Mr. Shinya Sugita and Ms. Aki Nemoto for their help with sample preparation. USIAS (University of Strasbourg), NSF, NIH, MEXT, CREST-JST, NRF

REFERENCES

- (1) Berndt, A.; Lee, S. Y.; Ramakrishnan, C.; Deisseroth, K. Structure-guided transformation of channelrhodopsin into a light-activated chloride channel. *Science* **2014**, *344*, 420–424.
- (2) Kralj, J. M.; Douglass, A. D.; Hochbaum, D. R.; Maclaurin, D.; Cohen, A. E. Optical recording of action potentials in mammalian neurons using a microbial rhodopsin. *Nat. Methods* **2012**, *9*, 90–95.
- (3) Gong, Y.; Wagner, M. J.; Li, J. Z.; Schnitzer, M. J. Imaging neural spiking in brain tissue using FRET-opsin protein voltage sensors. *Nat. Commun.* **2014**, *5*, 3674.
- (4) Kralj, J. M.; Hochbaum, D. R.; Douglass, A. D.; Cohen, A. E. Electrical Spiking in Escherichia coli Probed with a Fluorescent Voltage-Indicating Protein. *Science* **2011**, 333, 345–348.
- (5) Gong, Y.; Li, J. Z.; Schnitzer, M. J. Enhanced Archaerhodopsin Fluorescent Protein Voltage Indicators. *PLoS One* **2013**, 8, No. e66959.
- (6) Looger, L. L.; Griesbeck, O. Genetically encoded neural activity indicators. Curr. Opin. Neurobiol. 2012, 22, 18–23. Looger, L. L. Running in reverse: rhodopsins sense voltage. Nat. Methods 2012, 9, 43. Mutoh, H.; Akemann, W.; Knöpfel, T. Genetically engineered fluorescent voltage reporters. ACS Chem. Neurosci. 2012, 3, 585–592. McIsaac, R. S.; Engqvist, M. K. M.; Wannier, T.; Rosenthal, A. Z.; Herwig, L.; Flytzanis, N. C.; Imasheva, E. S.; Lanyi, J. K.; Balashov, S. P.; Gradinaru, V.; Arnold, F. H. Directed evolution of a far-red fluorescent rhodopsin. Proc. Natl. Acad. Sci. U. S. A. 2014, 111, 13034–13039.
- (7) Flytzanis, N. C.; Bedbrook, C. N.; Chiu, H.; Engqvist, M. K. M.; Xiao, C.; Chan, K. Y.; Sternberg, P. W.; Arnold, F. H.; Gradinaru, V. Archaerhodopsin variants with enhanced voltage-sensitive fluorescence in mammalian and Caenorhabditis elegans neurons. *Nat. Commun.* **2014**, *5*, 4894.
- (8) Hochbaum, D. R.; Zhao, Y.; Farhi, S. L.; Klapoetke, N.; Werley, C. A.; Kapoor, V.; Zou, P.; Kralj, J. M.; Maclaurin, D.; Smedemark-Margulies, N.; Saulnier, J. L.; Boulting, G. L.; Straub, C.; Cho, Y. K.; Melkonian, M.; Wong, G. K.-S.; Harrison, D. J.; Murthy, V. N.; Sabatini, B. L.; Boyden, E. S.; Campbell, R. E.; Cohen, A. E. Alloptical electrophysiology in mammalian neurons using engineered microbial rhodopsins. *Nat. Methods* **2014**, *11*, 825–833.
- (9) Maclaurin, D.; Venkatachalam, V.; Lee, H.; Cohen, A. E. Mechanism of voltage-sensitive fluorescence in a microbial rhodopsin. *Proc. Natl. Acad. Sci. U. S. A.* **2013**, *110*, 5939–5944.
- (10) Hou, J. H.; Venkatachalam, V.; Cohen, A. E. Temporal Dynamics of Microbial Rhodopsin Fluorescence Reports Absolute Membrane Voltage. *Biophys. J.* **2014**, *106*, 639–648.
- (11) Engqvist, M. K. M.; McIsaac, R. S.; Dollinger, P.; Flytzanis, N. C.; Abrams, M.; Schor, S.; Arnold, F. H. Directed Evolution of Gloeobacter violaceus Rhodopsin Spectral Properties. *J. Mol. Biol.* **2015**, 427, 205–220.
- (12) Piatkevich, K. D.; Jung, E. E.; Straub, C.; Linghu, C.; Park, D.; Suk, H.-J.; Hochbaum, D. R.; Goodwin, D.; Pnevmatikakis, E.; Pak, N. A robotic multidimensional directed evolution approach applied to fluorescent voltage reporters. *Nat. Chem. Biol.* **2018**, *14*, 352.

- (13) Herwig, L.; Rice, A. J.; Bedbrook, C. N.; Zhang, R. K.; Lignell, A.; Cahn, J. K. B.; Renata, H.; Dodani, S. C.; Cho, I.; Cai, L.; Gradinaru, V.; Arnold, F. H. Directed Evolution of a Bright Near-Infrared Fluorescent Rhodopsin Using a Synthetic Chromophore. *Cell Chem. Biol.* 2017, 24, 415–425. Hontani, Y.; Ganapathy, S.; Frehan, S.; Kloz, M.; DeGrip, W. J.; Kennis, J. T. M. Strong pH-Dependent Near-Infrared Fluorescence in a Microbial Rhodopsin Reconstituted with a Red-Shifting Retinal Analogue. *J. Phys. Chem. Lett.* 2018, 9, 6469.
- (14) Kawanabe, A.; Furutani, Y.; Jung, K. H.; Kandori, H. Photochromism of Anabaena sensory rhodopsin. *J. Am. Chem. Soc.* **2007**, *129*, 8644–8649.
- (15) Cheminal, A.; Léonard, J.; Kim, S. Y.; Jung, K.-H.; Kandori, H.; Haacke, S. Steady state emission of the fluorescent intermediate of Anabaena Sensory Rhodopsin as a function of light adaptation conditions. *Chem. Phys. Lett.* **2013**, *587*, 75–80.
- (16) Vogeley, L.; Sineshchekov, O. A.; Trivedi, V. D.; Sasaki, J.; Spudich, J. L.; Luecke, H. Anabaena sensory rhodopsin: a photochromic color sensor at 2.0 A. *Science* **2004**, *306*, 1390–1393.
- (17) Luk, H. L.; Melaccio, F.; Rinaldi, S.; Gozem, S.; Olivucci, M. Molecular bases for the selection of the chromophore of animal rhodopsins. *Proc. Natl. Acad. Sci. U. S. A.* **2015**, *112*, 15297–15302.
- (18) McIsaac, R. S.; Bedbrook, C. N.; Arnold, F. H. Recent Advances in Engineering Microbial Rhodopsins for Optogenetics. *Curr. Opin. Struct. Biol.* **2015**, 33, 8–15. Deisseroth, K. Optogenetics. *Nat. Methods* **2011**, 8, 26–29.
- (19) Jung, K.-H.; Trivedi, V. D.; Spudich, J. L. Demonstration of a sensory rhodopsin in eubacteria: Sensory rhodopsin in eubacteria. *Mol. Microbiol.* **2003**, *47*, 1513–1522. Choi, A. R.; Kim, S. Y.; Yoon, S. R.; Bae, K.; Jung, K.-H. Substitution of Pro206 and Ser86 residues in the retinal binding pocket of Anabaena sensory rhodopsin is not sufficient for proton pumping function. *J. Microbiol. Biotechnol.* **2007**, *17*, 138–145.
- (20) Gueye, M.; Nillon, J.; Crégut, O.; Léonard, J. Broadband UV-Vis vibrational coherence spectrometer based on a hollow fiber compressor. *Rev. Sci. Instrum.* **2016**, *87*, 093109.
- (21) Bradler, M.; Baum, P.; Riedle, E. Femtosecond continuum generation in bulk laser host materials with sub-μJ pump pulses. *Appl. Phys. B: Lasers Opt.* **2009**, *97*, 561–574.
- (22) Melaccio, F.; del Carmen Marín, M.; Valentini, A.; Montisci, F.; Rinaldi, S.; Cherubini, M.; Yang, X.; Kato, Y.; Stenrup, M.; Orozco-Gonzalez, Y.; Ferré, N.; Luk, H. L.; Kandori, H.; Olivucci, M. Toward Automatic Rhodopsin Modeling as a Tool for High-Throughput Computational Photobiology. *J. Chem. Theory Comput.* **2016**, *12*, 6020–6034.
- (23) Roos, B. O. In *Ab Initio Methods in Quantum Chemistry II*; Lawley, K. P., Ed.; Wiley & Sons: Chichester, 1987; pp 399–445.
- (24) Andersson, K.; Malmqvist, P. A.; Roos, B. O.; Sadlej, A. J.; Wolinski, K. Second-order perturbation theory with a CASSCF reference function. *J. Phys. Chem.* **1990**, *94*, 5483–5488.
- (25) Aquilante, F.; Autschbach, J.; Carlson, R. K.; Chibotaru, L. F.; Delcey, M. G.; De Vico, L.; Fernandez Galván, I.; Ferré, N.; Frutos, L. M.; Gagliardi, L.; Garavelli, M.; Giussani, A.; Hoyer, C. E.; Li Manni, G.; Lischka, H.; Ma, D.; Malmqvist, P.-Å.; Müller, T.; Nenov, A.; Olivucci, M.; Pedersen, T. B.; Peng, D.; Plasser, F.; Pritchard, B.; Reiher, M.; Rivalta, I.; Schapiro, I.; Segarra-Martì, J.; Stenrup, M.; Truhlar, D. G.; Ungur, L.; Valentini, A.; Vancoillie, S.; Veryazov, V.; Vysotskiy, V. P.; Weingart, O.; Zapata, F.; Lindh, R. Molcas 8: New capabilities for multiconfigurational quantum chemical calculations across the periodic table. *J. Comput. Chem.* **2016**, *37*, 506–541.
- (26) Ponder, J. W.; Richards, F. M. An efficient newton-like method for molecular mechanics energy minimization of large molecules. *J. Comput. Chem.* **1987**, *8*, 1016–1024.
- (27) Ferré, N.; Olivucci, M. Probing the Rhodopsin Cavity with Reduced Retinal Models at the CASPT2//CASSCF/AMBER Level of Theory. J. Am. Chem. Soc. 2003, 125, 6868–6869. Ferré, N.; Cembran, A.; Garavelli, M.; Olivucci, M. Complete-active-space self-consistent-field/Amber parameterization of the Lys296-retinal-

- Glu113 rhodopsin chromophore-counterion system. *Theor. Chem. Acc.* **2004**, *112*, 335–341.
- (28) Gozem, S.; Luk, H. L.; Schapiro, I.; Olivucci, M. Theory and Simulation of the Ultrafast Double-Bond Isomerization of Biological Chromophores. *Chem. Rev.* **2017**, *117*, 13502–13565.
- (29) Manathunga, M.; Yang, X.; Orozco-Gonzalez, Y.; Olivucci, M. Impact of Electronic State Mixing on the Photoisomerization Timescale of the Retinal Chromophore. *J. Phys. Chem. Lett.* **2017**, *8*, 5222–5227.
- (30) Michl, J.; Bonačić-Koutecký, V. Electronic Aspects of Organic Photochemistry; Wiley: New York, 1990.
- (31) Manathunga, M.; Yang, X.; Olivucci, M. Electronic State Mixing Controls the Photoreactivity of a Rhodopsin with All-trans Chromophore Analogues. *J. Phys. Chem. Lett.* **2018**, *9*, 6350–6355.
- (32) Bonačić-Koutecký, V.; Schöffel, K.; Michl, J. Critically heterosymmetric biradicaloid geometries of of protonated Schiff bases. *Theor. Chim. Acta* **1987**, 72, 459–474.
- (33) Agathangelou, D.; Orozco-Gonzalez, Y.; del Carmen Marín, M.; Roy, P. P.; Brazard, J.; Kandori, H.; Jung, K.-H.; Léonard, J.; Buckup, T.; Ferré, N.; Olivucci, M.; Haacke, S. Effect of point mutations on the ultrafast photo-isomerization of Anabaena sensory rhodopsin. *Faraday Discuss.* **2018**, 207, 55–75.
- (34) Kouyama, T.; Kinosita, K.; Ikegami, A. Excited-state dynamics of bacteriorhodopsin. *Biophys. J.* **1985**, *47*, 43–54.
- (35) Manathunga, M.; Yang, X.; Luk, H. L.; Gozem, S.; Frutos, L. M.; Valentini, A.; Ferré, N.; Olivucci, M. Probing the Photodynamics of Rhodopsins with Reduced Retinal Chromophores. *J. Chem. Theory Comput.* **2016**, *12*, 839–850.
- (36) Song, L.; El-Sayed, M. A.; Lanyi, J. K. Protein catalysis of the retinal subpicosecond photoisomerization in the primary process of bacteriorhodopsin photosynthesis. *Science* **1993**, 261, 891–894. Kennis, J. T. M.; Larsen, D. S.; Ohta, K.; Facciotti, M. T.; Glaeser, R. M.; Fleming, G. R. Ultrafast protein dynamics of bacteriorhodopsin probed by photon echo and transient absorption spectroscopy. *J. Phys. Chem. B* **2002**, 106, 6067–6080. Van Stokkum, I. H. M.; Gobets, B.; Gensch, T.; van Mourik, F.; Hellingwerf, K. J.; van Grondelle, R.; Kennis, J. T. M. (Sub)-picosecond spectral evolution of fluorescence in photoactive proteins studied with a synchroscan streak camera system. *Photochem. Photobiol.* **2006**, 82, 380–388.
- (37) Tahara, S.; Takeuchi, S.; Abe-Yoshizumi, R.; Inoue, K.; Ohtani, H.; Kandori, H.; Tahara, T. Origin of the Reactive and Nonreactive Excited States in the Primary Reaction of Rhodopsins: pH Dependence of Femtosecond Absorption of Light-Driven Sodium Ion Pump Rhodopsin KR2. J. Phys. Chem. B 2018, 122, 4784—4792. Hontani, Y.; Marazzi, M.; Stehfest, K.; Mathes, T.; Stokkum, I. H. M.; Elstner, M.; Hegemann, P.; Kennis, J. T. M. Reaction dynamics of the chimeric channelrhodopsin C1C2. Sci. Rep. 2017, 7, 7217. Dokukina, I.; Weingart, O. Spectral properties and isomerisation path of retinal in C1C2 channelrhodopsin. Phys. Chem. Chem. Phys. 2015, 17, 25142.
- (38) Muñoz-Losa, A.; Fdez Galván, I.; Aguilar, M. A.; Martín, M. E. Retinal models: comparison of electronic absorption spectra in the gas phase and in methanol solution. *J. Phys. Chem. B* **2008**, *112*, 8815–8823. Demoulin, B.; Altavilla, S. F.; Rivalta, I.; Garavelli, M. Fine Tuning of Retinal Photoinduced Decay in Solution. *J. Phys. Chem. Lett.* **2017**, *8*, 4407–4412. Munoz-Losa, A.; Ignacio, I.; Aguilar, M. A.; Martín, M. E. Simultaneous Solvent and Counterion Effects on the Absorption Properties of a Model of the Rhodopsin Chromophore. *J. Chem. Theory Comput.* **2013**, *9*, 1548–1556.
- (39) Nielsen, I. B.; Lammich, L.; Andersen, L. H. S1 and S2 Excited States of Gas-Phase Schiff-Base Retinal Chromophores. *Phys. Rev. Lett.* **2006**, *96*, 018304.